(This is a sample cover image for this issue. The actual cover is not yet available at this time.)

Journal of Non-Newtonian Fluid Mechanics 173–174 (2012) 72–86

Contents lists available at SciVerse ScienceDirect

Journal of Non-Newtonian Fluid Mechanics

journal homepage: http://www.elsevier.com/locate/jnnfm

Full two-dimensional rapid chute flows of simple viscoplastic granular materials with a pressure-dependent dynamic slip-velocity and their numerical simulations

Birte Domnik *, Shiva P. Pudasaini

Department of Geodynamics and Geophysics, Steinmann Institute, University of Bonn, Nussallee 8, D-53115 Bonn, Germany

ARTICLE INFO

Article history:
Received 15 December 2011
Received in revised form 1 March 2012
Accepted 2 March 2012
Available online 13 March 2012

Keywords:
Granular channel flow
Viscoplastic flows
Slip on rigid boundaries
Coulomb sliding law
Pressure-dependent dynamic slip velocity
Marker-and-cell methods

ABSTRACT

We present a fully two-dimensional, novel Coulomb-viscoplastic sliding model, which includes some basic features and observed phenomena in dense granular flows like the exhibition of a yield strength and a non-zero slip velocity. The interaction of the flow with the solid boundary is modelled by a pressure and rate-dependent Coulomb-viscoplastic sliding law. The bottom boundary velocity is required for a fully two-dimensional model, whereas in classical, depth-averaged models its explicit knowledge is not needed. It is observed in experiments and in the field that in rapid flow of frictional granular material down the slopes even the lowest particle layer in contact with the bottom boundary moves with a non-zero and non-trivial velocity. Therefore, the no-slip boundary condition, which is generally accepted for simulations of ideal fluid, e.g., water, is not applicable to granular flows. The numerical treatment of the Coulomb-viscoplastic sliding model requires the set up of a novel pressure equation, which defines the pressure independent of the bottom boundary velocities. These are dynamically and automatically defined by our Coulomb-viscoplastic sliding law for a given pressure. A simple viscoplastic granular flow down an inclined channel subject to slip or no-slip at the bottom boundary is studied numerically with the marker-and-cell method. The simulation results demonstrate the substantial influence of the chosen boundary condition. The Coulomb-viscoplastic sliding law reveals completely different flow dynamics and flow depth variations of the field quantities, mainly the velocity and full dynamic pressure, and also other derived quantities, such as the bottom shear-stress, and the mean shear-rate, compared to the commonly used no-slip boundary condition. We show that for Coulomb-viscoplastic sliding law observable shearing mainly takes place close to the sliding surface in agreement with observations but in contrast to the no-slip boundary condition.

1. Introduction

Granular flows play an important role in our daily life. They take place in form of geophysical and industrial mass flows and show very different phenomena. The flow of a granular avalanche is characterised by three different flow regimes: (i) the starting zone where rupture and fragmentation of the solid material occurs and/or the granular material begins to flow, (ii) the avalanching zone where the granular material reaches fast supercritical speed, and (iii) the run-out zone where the moving mass is decelerated and comes to a rather sudden standstill [1]. Observations, both in the laboratory and nature, show that after the flow release, flow transits from a subcritical to a supercritical regime. In further downstream, the rapid flow regime develops, which is characterised by fairly uniform velocity profiles with depth, strong shearing in the vicinity of the base and dominant sliding at the base [2]. In the deposition regime and, in particular, in the transition region from the rapid flow into the deposition zone shock-like structures form, and an overall depth flow changes into a surface boundary layer flow, which quickly slows down and eventually settles [1].

Depth-averaged model equations and simulations have been largely successful in describing the flows of granular materials, avalanches and debris flows down channels and slopes [2–4]. However, the depth-averaged equations are restricted to smooth basal surfaces and smooth changes of the slopes. Those equations could not fully be applied when topography changes are large (large curvatures), in the vicinity of the flow obstacle interactions, during the depositions, for strongly converging and diverging flows [5], in flow initiations and also during the deposition processes. All these complex processes can typically be characterised by the dominant basal slip, followed by the strong shearing and weak shearing of the velocity field from sliding surface to the top free surface of flow.

* Corresponding author.
E-mail address: domnik@geo.uni-bonn.de (B. Domnik).

0377-0257/$ - see front matter © 2012 Elsevier B.V. All rights reserved.
http://dx.doi.org/10.1016/j.jnnfm.2012.03.001

The most important physical quantities in avalanche and granular flow dynamics are the velocity and pressure distribution through the depth and along the slope, evolution of the geometry, and the deposition profile. From a structural engineering and planning point of view, one must properly predict the flow field and estimate impact pressures on civil structures that may be hit by an avalanche in order to adequately design buildings, roadways, and rail transportation in mountainous regions. Equally important is to know the depth and velocity evolution of flowing granular materials through various channels in process engineering scenarios. Therefore, in general, we need a physically complete description of the flow dynamics without reduction of the information through the flow depth.

A first step towards modelling such complicated three-dimensional flows is to reduce it to two dimensions by first studying the inclined chute flow to obtain detailed information on velocities and build up of deposition geometries. Some basic two-dimensional channel flow experiments and their simulations with depth-averaged model equations are reported in [1,6,7]. In this paper, we are concerned with the development of a new theoretical model and simulation results in the first two regimes (starting and avalanching zone), which can also be extended in the third (depositional) regime. Here we advance fundamentally and substantially as compared with the classical granular flow and avalanche models. We retain all the information of the physics of flow by developing a full-dimensional model (at the moment for channel flow, that will later be extended for the fully three-dimensional flows) and then directly solving the model equation without reducing the dimension.

Depending on the flow configuration, granular deformation may behave as an elastic, plastic, or viscous material, or the combination of them [2,8–10]. In this paper, we will model the internal deformation as a simple viscoplastic material with a constant yield strength. Another important aspect of granular flow simulation is the basal boundary condition. In the classical depth-averaged modelling, due to the depth-averaging, explicit knowledge of the basal boundary is not needed. However, for the full-dimensional treatment of the flow, we need to explicitly supply the bottom and the free surface boundary conditions, which automatically evolves in time and space. In the fluid-dynamic approach the no-slip boundary condition, in which the slip velocity is set to zero, is widely and successfully used in many fluid simulations [11–14]. However, it is observed in experiments and in the field that in rapid flow of granular material down the slopes, even the lowest particle layer in contact with the bottom boundary moves with a non-zero and non-trivial velocity [1,2,15–20]. The flow of granular material is not the only situation, in which the no-slip condition is no longer appropriate. Also in polymer-processing different attempts were made to formulate boundary conditions which allow partial slip at rigid boundaries [21,22]. Generally, the no-slip condition works well for a single-component fluid, a wetted surface, and low levels of shear-stress [23]. This is not the case, when non-absorbing polymers are dissolved in fluids of lower viscosity or in the case of granular flows, in which the interstitial fluid (e.g., air) between the particles can play the role of the fluid with low viscosity. Also Navier was not satisfied with the no-slip boundary condition and proposed a slip-condition, in which a constant ς is introduced to describe the slip velocity u^b [22]: $\varsigma u^b = \nu[\partial\, u_t/\partial n]^b$, where ν is the viscosity, u_t is the tangential fluid velocity, n is the normal of wall boundary directed into the fluid, and the ratio ν/ς has the dimension of a length. We want to continue with Navier's idea of a slip velocity at the wall boundary, but by relating the normal pressure to the shear-stress on the wall and so generating a slip velocity as observed in rapid granular flows. This is an entirely novel and innovative concept in rapid granular flows. The problem with Navier's slip is that it produces also a high shearing in fast but thin flows with low normal pressures on the wall, what is not observed in rapid granular flows [1,17]. Therefore, we are using the Coulomb sliding law to relate the shear-stress T^b to the normal stress N^b at the bottom sliding surface (b): $T^b = \tan\delta N^b$, where δ is the bed friction angle. The Coulomb sliding law has successfully been used to model friction in many depth-averaged simulations of rapid granular flows [2–7,17,24–26]. Platzer et al. showed that the relation between the normal and shear-stress in dense snow avalanches can be described by a Coulomb friction law, in which cohesion has to be taken into account especially for wet snow avalanches [19]. Uhland also utilised the Coulomb friction law to describe the slip velocity of a plastic melt flow through a pipe of circular cross-section [27]. The stress–strain behaviour is described by a viscous power law. He assumed a steady, non-accelerated (no gravitational acceleration), one-dimensional (no radial component) flow. Based on these assumptions, which do not hold in general and in particular for rapid granular flows, he presented analytical solutions for the flow velocity and pressure. However, his velocity solution does not satisfy the continuity equation.

First, we will develop a novel Coulomb frictional basal slip model, which uses the Coulomb friction law to model the interaction of the flow with the solid basal boundary surface. Formulation of the new pressure equation is presented in terms of finite differences for both pressure-independent and pressure-dependent basal slips. Afterwards, we study three different basal boundary conditions: no-slip, free-slip (pressure-independent), and the Coulomb-type slip (pressure-dependent) at the base. The observed differences in the flow dynamics for the no-slip and free-slip boundary conditions and the Coulomb sliding law are discussed in detail. The flow dynamics include the novel modelling and simulation of the evolution of the pressure and velocity field through the flow depth and the depth profile itself.

2. A simple viscoplastic granular flow model with slip

2.1. Field equations

The motion of granular material in a two-dimensional inclined rectangular channel (Fig. 4) is characterised by the pressure p and the velocity $\mathbf{u} = (u, w)^T$, with u the velocity component in downslope direction (x) and w the velocity component perpendicular to the channel surface (z). Incompressible flow is assumed, so density changes are negligible [2]. The flow in a channel inclined by an angle ζ is described by a system of partial differential equations, representing the mass and momentum balances:

$$\mathrm{div}\mathbf{u} = 0, \tag{1}$$

$$\frac{d\mathbf{u}}{dt} = \mathrm{div}\boldsymbol{\sigma} + \mathbf{g}, \tag{2}$$

where $\boldsymbol{\sigma}$ is the Cauchy stress tensor normalised by density, $\mathbf{g}(\zeta) = (g\sin\zeta,\ -g\cos\zeta)^T$ is the gravitational acceleration with the gravity constant g, and d/dt is the material derivative.

We are considering a dry dense granular material, which is assumed to be described by a viscoplastic fluid [9,10,28–30]. The normalised stress tensor for a viscoplastic fluid can be written as

$$\boldsymbol{\sigma} = -p\mathbb{1} + 2\nu_{\mathrm{eff}}\mathbf{D}, \tag{3}$$

where p is the normalised pressure, the strain rate tensor is given by the symmetric part of the velocity gradient, $\mathbf{D} = 1/2[(\nabla\mathbf{u}) + (\nabla\mathbf{u})^T]$, and ν_{eff} is the effective kinematic viscosity, which is defined by

$$\nu_{\mathrm{eff}} = \nu + \frac{\tau_0}{\|\mathbf{D}\|}[1 - \exp(-m\|\mathbf{D}\|)]. \tag{4}$$

The effective kinematic viscosity depends on the kinematic viscosity ν, the yield stress τ_0 (normalised by density), and the norm of

the strain rate tensor, defined as $\|\mathbf{D}\| = \sqrt{2\mathrm{tr}(\mathbf{D}^2)}$. With the introduction of the exponential factor, $[1-\exp(-m\|\mathbf{D}\|)]$, (4) holds uniformly in yielded and unyielded regions, and the transition between these regions is smoother for smaller exponents m [31]. (We used $m = 100$ for the simulations presented in Section 4.) For $\tau_0 = 0$ the effective viscosity equals the viscosity ν, and the material behaves as a Newtonian fluid. For simplicity, we assume a constant Bingham yield stress. In applications, this simple viscoplastic rheology is often an adequate choice [32–35]. Then shearing within the material is induced by friction at the rigid boundaries through the boundary conditions. If shearing, which results from direct contacts between the granular particles, becomes considerable, the assumption of a constant yield stress could be too simple and a pressure dependent yield stress should have been considered like in [30,36]. This, however, is not within the scope of this work.

With the notations

$$F = -\partial_x(u^2) - \partial_z(uw) + 2\partial_x(\nu_{\mathrm{eff}}\partial_x u) + \partial_z[\nu_{\mathrm{eff}}(\partial_z u + \partial_x w)] + g\sin(\zeta), \tag{5}$$

$$G = -\partial_z(w^2) - \partial_x(uw) + 2\partial_z(\nu_{\mathrm{eff}}\partial_z w) + \partial_x[\nu_{\mathrm{eff}}(\partial_z u + \partial_x w)] - g\cos(\zeta), \tag{6}$$

the momentum Eq. (2) can now be expressed as

$$\partial_t u = F - \partial_x p, \tag{7}$$

$$\partial_t w = G - \partial_z p. \tag{8}$$

Eqs. (7) and (8) are integrated numerically to compute the velocities u and w. To calculate the pressure, a Poisson equation for the pressure is derived by applying ∂_x or ∂_z on the x or z-momentum-conservation Eqs. ((7) and (8)), adding both resulting equations, and using the continuity Eq. (1) to yield:

$$\Delta p = \partial_x^2 p + \partial_z^2 p = \partial_x F + \partial_z G. \tag{9}$$

Eqs. (7)–(9) require appropriate boundary conditions for the velocities at the free surface and basal surface, which is one of the main focuses of this article.

2.2. Velocity boundary condition at the base

In the following, the friction induced by the movement of granular material on sliding planes, that can be at rigid boundaries with an inner normal vector $\mathbf{n}$ and a tangential vector $\mathbf{t}$, is considered. In rapid flows of granular material down the slopes, even the lowest particle layer in contact with the bottom boundary moves with a non-zero and non-trivial velocity. Therefore, the generally used no-slip boundary condition does not represent the flow physics. A non-zero slip velocity is determined by the frictional strength, which depends on the load the material exerts on the rigid boundary. So, it is natural to relate the shear-stress $T^b = \boldsymbol{\sigma}^b\mathbf{n}\cdot\mathbf{t}$ to the normal pressure $N^b = -\boldsymbol{\sigma}^b\mathbf{n}\cdot\mathbf{n}$ at the sliding surface (b). This can be achieved by using the Coulomb sliding law, which was already successfully used in simulations of rapid granular flows:

$$T^b = \frac{u^b}{|u^b|}\tan\delta N^b. \tag{10}$$

This relation asserts that a material yields plastically if the shear-stress attains the critical value given by (10). The tangent of the bed friction angle δ defines the proportionality constant and higher values of δ go along with a higher shearing and, therefore, with a higher frictional force at the rigid boundary. To guarantee that the frictional force is always opposite to the direction of motion, the factor $u^b/-u^b-$ is introduced. The flowing granular material does not penetrate through the boundary, so $\mathbf{n}\cdot\mathbf{u}^b = 0$ and also $[(\mathbf{t}\cdot\nabla)(\mathbf{n}\cdot\mathbf{u})]^b = 0$. Therefore, from (3), with a bit of algebra, the normal and shear stresses at the bottom are given by $N^b = p^b + 2\nu_{\mathrm{eff}}^b[(\mathbf{t}\cdot\nabla)(\mathbf{t}\cdot\mathbf{u})]^b$ and $T^b = \nu_{\mathrm{eff}}^b[(\mathbf{n}\cdot\nabla)(\mathbf{t}\cdot\mathbf{u})]^b$, which leads to a pressure and rate-dependent Coulomb-viscoplastic sliding law expressed in terms of the tangential velocity and the pressure at the boundary

$$[(\mathbf{n}\cdot\nabla)(\mathbf{t}\cdot\mathbf{u})]^b - 2c^{\mathrm{F}}[(\mathbf{t}\cdot\nabla)(\mathbf{t}\cdot\mathbf{u})]^b = \frac{c^{\mathrm{F}}}{\nu_{\mathrm{eff}}^b}p^b. \tag{11}$$

Here the 'friction factor', c^{F}, is defined by

$$c^{\mathrm{F}} = \begin{cases} \frac{u^b}{|u^b|}\tan\delta, & u^b \neq 0, \\ 0, & u^b = 0. \end{cases} \tag{12}$$

The ratio between the grain friction, c^{F}, and the viscous friction is called the 'effective friction ratio':

$$F_e^r = \frac{c^{\mathrm{F}}}{\nu_{\mathrm{eff}}^b}. \tag{13}$$

The pressure and rate-dependent Coulomb-viscoplastic sliding law, (11), dynamically and automatically defines the bottom boundary velocity $[\mathbf{t}\cdot\mathbf{u}]^b$. Note that in the classical, depth-averaged plastic flow models for granular material N^b is the overburden pressure (material normal load), i.e., the hydrostatic pressure, which is independent of the flow dynamics. Then, the Coulomb sliding law, (10), does not include any dynamic information about the flow and deformation, such as the velocity and pressure. So, (10) is then a rate-independent plastic law.

It is important to observe that if the Coulomb friction coefficient c^{F} equals zero ($\delta = 0$ or no material motion), then no grain friction exists and (11) reduces to the well-known free-slip condition $[(\mathbf{n}\cdot\nabla)(\mathbf{t}\cdot\mathbf{u})]^b = 0$, for which no friction at the boundary is present and, therefore, the basal shear-stress equals zero.

For negligible granular friction or for very high effective viscosity (in both cases $F_e^r \approx 0$), the pressure dependency is lost, and (11) becomes

$$\left[\frac{(\mathbf{n}\cdot\nabla)(\mathbf{t}\cdot\mathbf{u})}{(\mathbf{t}\cdot\nabla)(\mathbf{t}\cdot\mathbf{u})}\right]^b = 2c^{\mathrm{F}}. \tag{14}$$

So, the friction factor in terms of the bed friction angle defines the ratio between the normal and tangential derivative of the tangential velocity at the bottom. In the following, we will treat the more general case where the bottom pressure is not negligible (i.e. $F_e^r \neq 0$).

We are considering the motion of granular material in a narrow rectangular inclined channel with the main flow direction parallel to the x-axis. The main shearing occurs at the bottom boundary with the basal normal vector parallel to the z-direction ($\mathbf{n} = (0, 1)^T$, $\mathbf{t} = (1, 0)^T$). The shearing at the sidewalls has only a marginal influence on the granular flow and will be neglected [1,6]. Then the Coulomb shear-stress at the bottom, (10), can simply be written as

$$T^b = c^{\mathrm{F}}\left(p^b + 2\nu_{\mathrm{eff}}^b[\partial_x u]^b\right). \tag{15}$$

If the strain-rate approaches zero, the shear-stress is given by $T^b = c^{\mathrm{F}}p^b$. Hence, the Coulomb-viscoplastic friction law defines a yield criterion with a pressure dependent yield-stress. This describes the frictional nature of the interaction of the granular material with the rigid boundary. An increase in $\partial_x u$ results (due to continuity) in a higher bottom normal stress and, consequently, in a higher frictional bottom shear-stress (15). This is different for shear-stresses within the material, which will decrease due to a decline of the effective Bingham viscosity (4).

The Coulomb-viscoplastic sliding law, (11), for the rectangular inclined channel is given by

$$[\partial_z u]^b - 2c^F[\partial_x u]^b = \frac{c^F}{\nu^b_{\text{eff}}} p^b. \tag{16}$$

Eq. (16) is an equation for pressure in terms of the velocity gradients or vice versa.

In the following, (16) will be used as pressure-dependent velocity boundary condition at the sliding surface. Note that with (16) the bottom shear-stress depends on the normal stress contrary to Navier's slip and the no-slip boundary condition, in which it depends only on the velocity near the sliding surface.

3. Numerical method

3.1. Discretization and modelling of the free surface granular flows

In order to compute the velocities and the pressure from Eqs. (7)–(9), an appropriate discretization has to be carried out. Our numerical method is based on *NaSt2D* [12], a computer code using the finite-volume method for the simulation of incompressible Newtonian fluids. Following [12,37], we introduce a staggered grid (see, Fig. 1), in which the velocities and the pressure are not located at the same grid points to avoid possible pressure oscillations. The pressure p is located in the cell centres ('p-grid'), the x-velocity u in the midpoint of the vertical cell edges ('u-grid') and the z-velocity w in the midpoint of the horizontal cell edges ('w-grid'). To describe the boundary conditions a boundary strip is added at $i = 0$, $i = i_{\max} + 1$, $j = 0$ and $j = j_{\max} + 1$ (Fig. 2). Therefore, the whole grid consists of $(i_{\max} + 2) \cdot (j_{\max} + 2)$ cells $C_{i,j}$ with $i \in [0,\ i_{\max} + 1]$ and $j \in [0,\ j_{\max} + 1]$. The length of one single cell is $dx(dz)$ in $x(z)$-direction.

The Poisson Eq. (9) is discretized on the p-grid, and the $x(z)$-momentum Eqs. (7) and (8) are discretized on the $u(w)$-grid. The spatial derivatives are replaced by centred differences except for the convective terms, which are discretized by using a mixture of central differences and the donor-cell discretization. To discretize the time derivatives, we use first-order difference quotients.

To simulate and visualise the rapid free surface flow of frictional granular material, the marker-and-cell method is applied, in which marker-particles are used to determine whether a cell contains 'fluid' or not (see, Fig. 2), [37–39].

The originality of our approach is also due to the fact that we numerically implement the Coulomb-viscoplastic sliding law, which is presented in Section 3.3.

3.2. Pressure calculation for a pressure-independent basal slip

If a pressure-independent friction law such as the no-slip or free-slip condition is used, the velocity boundary conditions are known before calculating the pressure. In case of the no-slip condition, the tangential velocities should vanish at the boundary, e.g., for the bottom boundary at $z = 0$ (by using linear interpolation) the condition reads: $(u_{i,1} + u_{i,0})/2 = 0$. This is achieved by setting $u_{i,0} = -u_{i,1}$. The free-slip condition requires the normal derivative of the velocity component tangential to the boundary to vanish.

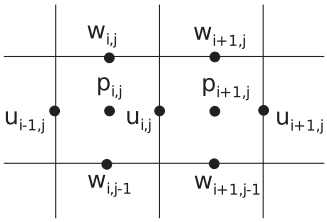

Fig. 1. Staggered grid. The pressure p is located in the cell centres and the $x(z)$-velocity $u(w)$ in the midpoint of the vertical (horizontal) cell edges.

For example, the free-slip boundary condition can be written as, $(u_{i,1} - u_{i,0})/dz = 0$, for the bottom boundary at $z = 0$ by using central differences. This leads to the velocity boundary condition $u_{i,0} = u_{i,1}$. Together with the condition for the normal velocities, $w_{i,0} = 0$, which asserts that the material cannot penetrate through a rigid boundary, the right hand side of the Poisson Eq. (9), is fixed for a given velocity field. Using central finite differences, (9) results in the discrete Poisson equation for the pressure p:

$$\frac{p_{i+1,j} - 2p_{i,j} + p_{i-1,j}}{dx^2} + \frac{p_{i,j+1} - 2p_{i,j} + p_{i,j-1}}{dz^2} = \left(\frac{F_{i,j} - F_{i-1,j}}{dx} + \frac{G_{i,j} - G_{i,j-1}}{dz}\right). \tag{17}$$

Eq. (17) can also be written as a system of N linear equations,

$$\mathbf{M}\mathbf{p} = \mathbf{b}, \tag{18}$$

with $\mathbf{M} \in \mathbb{R}^{N\times N}$ and $\mathbf{p}, \mathbf{b} \in \mathbb{R}^N$, where N is given by the number of inner 'fluid' cells. The matrix $\mathbf{M}$ depends only on the grid refinement. The right-hand-side of (18), $\mathbf{b}$, contains the spatial derivatives of the convective, diffusive and gravitational forces. Note that $\mathbf{M}$ is symmetric and negative definite and the system of linear equations can be solved for the pressure, e.g., with the successive overrelaxation (SOR) method [40].

After the pressure is calculated with the discrete Poisson Eq. (18), the momentum Eqs. ((7), (8)) are used to calculate the velocities for the next time step.

3.3. Pressure calculation for a pressure-dependent basal slip

If a pressure-dependent friction law, i.e., slip velocity at the base, is used for the rigid boundaries, (18) cannot be used for the pressure computation, because the vector $\mathbf{b}$ depends on the velocity boundary values, consequently, also on the pressure. Therefore, a pressure equation has to be formulated, which guarantees that the pressure satisfies both the Poisson equation and the pressure-dependent friction law at the bed. For this reason, here we develop a completely new approach, which is a fundamental contribution and an advancement in granular flow simulations from a computational point of view with ample applications in geophysical and industrial mass flows.

3.3.1. Coulomb sliding law

With the following discretizations at the lower right corner of a cell $C_{i,j}$ adjacent to a boundary cell $C_{i,j-1}$ (see, Fig. 3)

$$c^F \equiv \begin{cases} \frac{u_{i,j}}{|u_{i,j}|} \tan\delta, & u_{i,j} \neq 0, \\ 0, & u_{i,j} = 0, \end{cases} \tag{19}$$

$$p^b \equiv \frac{1}{2}(p_{i,j} + p_{i+1,j}), \tag{20}$$

$$[\partial_z u]^b \equiv \frac{1}{dz}\left(u_{i,j} - u^b_{i,j-1}\right), \tag{21}$$

$$[\partial_x u]^b \equiv \frac{1}{4dx}\left(u_{i+1,j} + u^b_{i+1,j-1} - u_{i-1,j} - u^b_{i-1,j-1}\right), \tag{22}$$

the Coulomb-viscoplastic sliding law, (16), can be expressed in terms of the bottom boundary values $u^b_{i,j}$

$$u^b_{i,j-1} + c^u_{i,j}\left(u^b_{i+1,j-1} - u^b_{i-1,j-1}\right) = u_{i,j} - c^u_{i,j}(u_{i+1,j} - u_{i-1,j}) - c^p_{i,j}(p_{i,j} + p_{i+1,j}), \tag{23}$$

with $c^u_{i,j} = \frac{1}{2}\frac{dz}{dx}c^F_{i,j}$ and $c^p_{i,j} = \frac{1}{2}dz c^F_{i,j}/\nu^{i,j}_{\text{eff}}$. Note that the discretization of c^F at $z = dz/2$, instead at the bottom ($z = 0$), is not critical, because only the sign of the tangential velocity is required, which is not expected to change within a half cell height. The pressure at the bottom is approximated by the next available pressure values. To

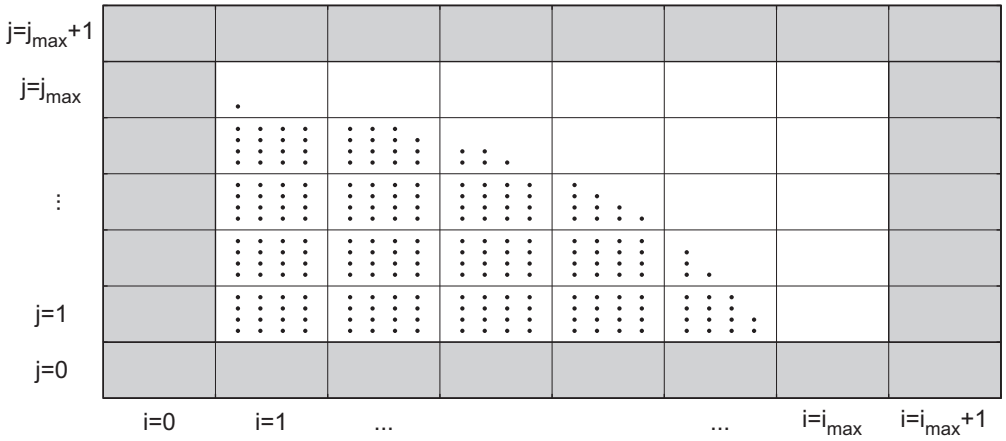

Fig. 2. Flow domain including marker particles and boundary strip. Cells in the boundary strip are called boundary cells.

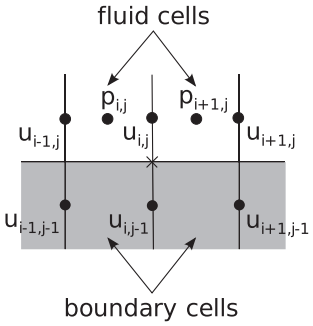

Fig. 3. Discretization points (cross) of Coulomb sliding law. If the cells $C_{i,j}$ and $C_{i+1,j}$ are 'fluid' cells and the cells $C_{i,j-1}$ and $C_{i+1,j-1}$ are boundary cells, the cell $C_{i,j}$ is called a Coulomb cell.

compute the velocity derivatives, central differences are used and for $[\partial_x u]^b$ averaging is performed additionally as mentioned in (22).

The Coulomb sliding law (23) can only be used to compute the bottom boundary velocity $u^b_{i,j-1}$ for cell $C_{i,j}$ if both cells $C_{i,j-1}$ and $C_{i+1,j-1}$ are boundary cells and both cell $C_{i,j}$ and also its right neighbouring cell $C_{i+1,j}$ contain 'fluid'. Then the cell $C_{i,j}$ is called a Coulomb cell, Fig. 3. Therefore, (23) requires boundary values near the free surface, which are given by the traction free condition of the free surface.

Eq. (23) can be written as a system of N^c linear equations

$$\mathbf{A}\mathbf{u}^b = \mathbf{b}_c - \mathbf{B}\mathbf{p}, \tag{24}$$

with $\mathbf{A} \in \mathbb{R}^{N^c \times N^c}$, $\mathbf{B} \in \mathbb{R}^{N^c \times N}$, $\mathbf{b}_c$ and $\mathbf{u}^b \in \mathbb{R}^{N^c}$, where N^c is given by the number of Coulomb cells. The matrix $\mathbf{A}$ is invertible, therefore, the velocity boundary values are calculable with (24) after the pressure computation. For $c^F = 0$ (no grain friction) the matrix $\mathbf{A}$ equals the identity matrix and for $c^F \neq 0$ its off-diagonal elements are proportional to c^u. The elements of $\mathbf{B}$, with which the pressure is multiplied, are given by c^p. Therefore, the increase of both the bottom pressure and the effective friction ratio leads to a decrease of the bottom velocity for an accelerating flow. This is a characteristic of the flow of frictional granular material.

3.3.2. Pressure equation

The pressure must satisfy both the Poisson Eq. (18) and the friction law (24), which both depend on the bottom velocities. Therefore, a central and novel idea is that these equations can be combined into a single pressure equation, which is independent of the bottom velocity.

The inhomogeneity $\mathbf{b}$ of the Poisson Eq. (18) contains F and G (compare with (17)), which are given by (5) and (6) and depend on the boundary velocities. The knowledge of the bottom velocity is necessary for the computation of the derivative $\partial_z^2 u$ in F, which can be expressed for cell $C_{i,j}$ in terms of the bottom boundary velocity $u^b_{i,j-1}$:

$$F_{i,j} = f^{(1)}_{i,j} u^b_{i,j-1} + f^{(2)}_{i,j}, \tag{25}$$

whereas $f^{(1)}_{i,j}$ and $f^{(2)}_{i,j}$ depend on the discretization and can be calculated without the knowledge of the bottom boundary velocity. With (17) and (25) $\mathbf{b}$ can now directly be related to the bottom boundary velocity:

$$\mathbf{b} = \mathbf{Q}\mathbf{u}^b + \mathbf{q}, \tag{26}$$

with $\mathbf{Q} \in \mathbb{R}^{N \times N^c}$ and $\mathbf{q} \in \mathbb{R}^N$. The vector $\mathbf{q}$ contains the boundary velocity-independent terms of the spatial derivatives of the convective and diffusive forces. The boundary velocity-dependent terms are included in $\mathbf{Q}\mathbf{u}^b$. Hence, the Poisson Eq. (18) can be written explicitly in terms of the bottom boundary velocity

$$\mathbf{M}\mathbf{p} = \mathbf{Q}\mathbf{u}^b + \mathbf{q}. \tag{27}$$

Combining (27) with (24) gives an equation for the pressure, which unlike (18) no longer requires the knowledge of bottom boundary velocities (this is a great advantage):

$$\underbrace{(\mathbf{M} + \mathbf{Q}\mathbf{A}^{-1}\mathbf{B})}_{\mathbf{L}}\mathbf{p} = \underbrace{\mathbf{Q}\mathbf{A}^{-1}\mathbf{b}_c + \mathbf{q}}_{\mathbf{b}_L}, \tag{28}$$

where the sparse pressure matrix $\mathbf{L} \in \mathbb{R}^{N \times N}$ and the vector $\mathbf{b}_L \in \mathbb{R}^N$ are defined. Note that, in general, the pressure matrix $\mathbf{L}$ is not symmetric, because $\mathbf{Q}\mathbf{A}^{-1}\mathbf{B}$ is not symmetric. The pressure matrix $\mathbf{L}$ depends on the Coulomb friction coefficient and the grid refinement. The right-hand-side of (28), $\mathbf{b}_L$, contains, on the one hand, the boundary velocity-independent terms of the spatial derivatives of the convective and diffusive forces and, on the other hand, velocity-dependent terms, which originate from the Coulomb sliding law, (24), and hence are also affected by the Coulomb friction coefficient.

For a vanishing Coulomb friction coefficient, $c^F = 0$, (28) reduces to the Poisson Eq. (18), because $\mathbf{A} = \mathbb{1}$, $\mathbf{B} = \mathbf{0}$ and $\mathbf{b}_c = \mathbf{u}^b$ according to (24). In this case, the velocity boundary condition equals the one for the free-slip boundary condition. For the more general case, $c^F \neq 0$, the bottom shear-stress depends on the bottom normal stress, i.e., the bottom pressure and derivative of the tangential velocity in downslope direction, but not on the velocity itself. Therefore, the new Coulomb-viscoplastic sliding law (16), differs

substantially from the no-slip boundary condition, for which the bottom shear-stress is velocity-dependent.

The Coulomb friction law is implemented by solving (28) for the pressure and obtaining the bottom boundary velocities according to (24) afterwards. So, we simultaneously have both the pressure and the slip-velocity at the bottom. It is worth mentioning that combination of the viscoplastic and Coulomb law made it possible to obtain (analytical or theoretical) expressions for both the pressure and the basal-slip velocity. For pressure-independent no-slip and free-slip boundary conditions the Poisson Eq. (18) is used instead of (28). In the following, benchmark simulations are performed in which no-slip, free-slip and Coulomb-slip are implemented and analysed. These simulations demonstrate the applicability of the new Coulomb-viscoplastic rheology and the performance of our new numerical method.

4. Granular flow simulations for different basal friction laws

4.1. Flow configuration and parameters

Here, we simulate the fully two-dimensional rapid simple viscoplastic granular flow down an inclined channel with an open end for different basal friction laws. The channel is 1m long, has an inclination of $\zeta = 45°$, and it is continuously fed from a silo, see Fig. 4. The inlet height is $h^{in} = 15$ cm and the mean inlet velocity is $\bar{u}^{in} = 0.9\ \mathrm{ms}^{-1}$. These flow configurations are similar to those used in [1,6,7]. To achieve realistic inflow conditions, the inflow velocity is varied exponentially with the flow depth: $u^{in}(z) = -\kappa[\alpha - \exp(\beta z)]$ with $\alpha = 1000$, $\beta = 45.9$, and $\kappa = 1.05 \times 10^{-3}$ (with appropriate dimensions) so that $\bar{u}^{in} = 0.9\ \mathrm{ms}^{-1}$. With this choice, the inlet velocity changes only slightly with depth until z is close to the inlet height, where u^{in} drops to almost zero, because of influence of the upper tip of the inlet gate. This is an observable phenomenon in silo-discharge. Note that the variation of the inlet velocity along the flow depth has only a slight impact on the overall flow characteristics, because immediately after the material has entered the channel it is subject to strong deformations. Setting the inlet velocity at the upper tip of the inlet gate to zero mainly affects the formation of the free surface in the vicinity of the flow front. The dynamic viscosity of mass flows events, like natural rock avalanches, debris avalanches and debris flows, can range from 0.01 to 20 Pa s or even more [41–43]. In the simulation we use a value of 15 Pa s, which corresponds to a kinematic viscosity of $\nu = 0.01\ \mathrm{m}^2\ \mathrm{s}^{-1}$ for a bulk density of $\rho = 1500\ \mathrm{kg\ m}^{-3}$. The estimated value of the lower limit of the yield stress for a rock avalanche is about 15 kPa. This holds for an assumed flow depth of about 5 m, a true rock density of about 3000 kg m^{-3}, and a friction coefficient about 0.7 [44,45]. In our numerical simulations the representative flow depth (along the channel) is 0.065 m, and the friction coefficient is about 0.5 (for a basal friction angle of 25°). Together with the assumed granular bulk density the yield stress can be estimated to 60 Pa, as used in the present simulation. However, here these numbers are taken mainly for the simulation purpose. So, depending on specific flow situation and the materials in use, the actual values of these physical parameters may deviate substantially from those used here. To study the role of the Coulomb friction and other basal sliding laws numerically, we present results for quasi-steady-state and complete transient channel flows. The physical variables are non-dimensionalised by using the scalings (following [2])

$$(x, z, t, u, p) = (L\hat{x}, H\hat{z}, T\hat{t}, U\hat{u}, P\hat{p}) \tag{29}$$

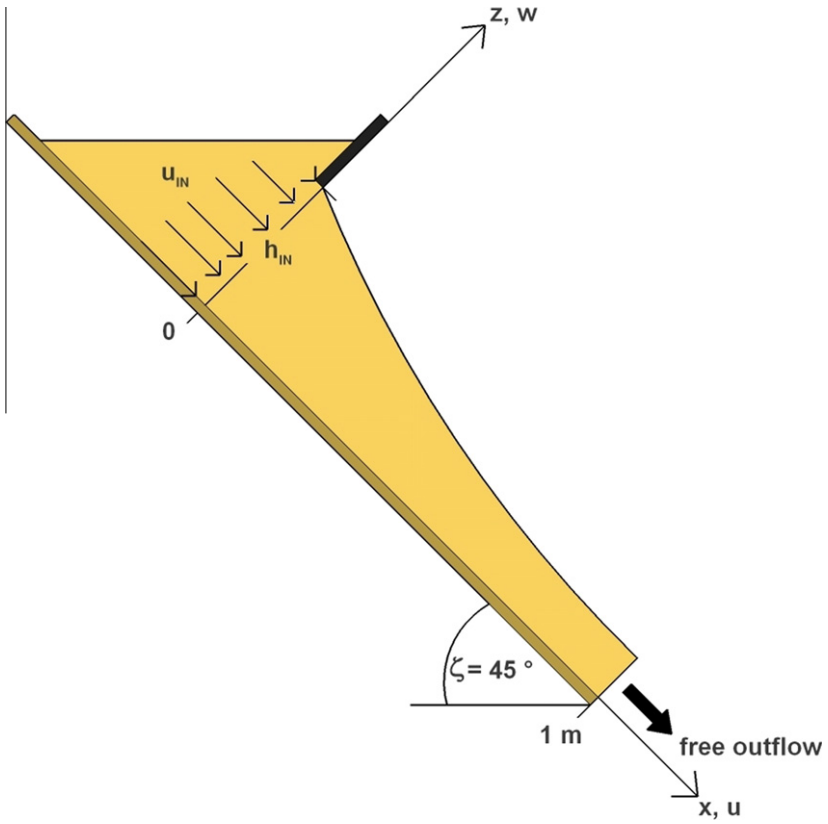

Fig. 4. Side view of the inclined chute used for the simulation of rapid channel flow of granular material with free outflow. The material enters into the channel at $x = 0$ with an inlet height of $h^{in} = 15$ cm and an average inlet velocity of $\bar{u}^{in} = 0.9\ \mathrm{ms}^{-1}$. The computational domain is [0, 1] m. The inlet velocity varies exponentially from the top of the opening gate to the bottom sliding surface and is indicated by the arrows at $x = 0$. ζ is the inclination angle of the channel.

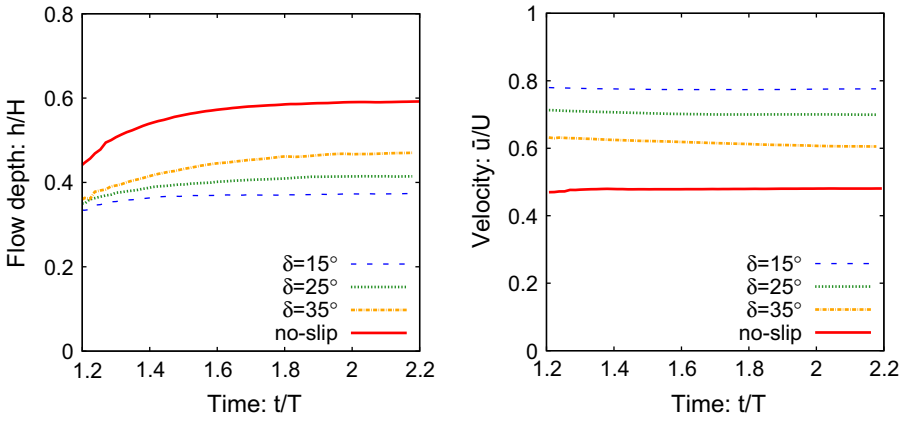

(a) Flow depth. (b) Mean velocity.

Fig. 5. Time dependence of characteristic flow quantities: depth (a) and mean velocity (b) (considered at $\hat{x} = 0.5$) for different basal friction laws.

where $T = \sqrt{L/g}$, $U = \sqrt{gL}$, and $P = \rho gH$. The hats represent non-dimensional variables. The channel length is chosen as typical length, $L = 1$ m, and the inlet height is taken as typical depth, $H = 0.15$ m.

4.2. Channel flow simulations

4.2.1. Quasi-steady-state flow

In the following, the simulated flows are considered at an instant of time, when the flow is in a quasi-steady-state. Fig. 5a and b show that for all considered friction laws the quasi-steady-state is attained well for $\hat{t} > 2$. For the no-slip simulation the chosen time is $\hat{t}^{\text{sim}} = 2.5$ and for the other simulations (free-slip and Coulomb friction laws) $\hat{t}^{\text{sim}} = 2.2$.

Fig. 6 shows the simulated flow depth (in background grey) and velocity vectors throughout the channel for three different basal friction laws. For the flow obeying the no-slip boundary condition (panel a), a strong shearing along the whole channel is observed contrary to the flow obeying the free-slip condition (panel b), which does not show a structured evolution of the velocity along depth but the velocity profile is uniform over depth. The simulation using the pressure-dependent Coulomb sliding law (panel c) differs substantially from both the no-slip and the free-slip simulations. It produces a clear and strong shear profile through a substantial flow depth in the vicinity of the bottom with a non-zero slip velocity at the bottom, which increases along the downslope channel position. However, the shear-rate is decreased and is close to zero in the upper half flow-depth and in the vicinity of the free surface.

These simulation results reveal that although the same internal viscoplastic flow rheologies, traction-free conditions, and inlet outlet conditions are applied for all three types of simulations, the results and flow patterns (flow depth, velocity and pressure patterns; are discussed in more detail later) are fundamentally different in the three panels. This means that the bottom boundary condition is an important mechanism to control and describe the flow dynamics in rapid granular flows in steep channels. Experiments in rapid granular flows in inclined chutes and channels show that the material slips along the channel (so, panel (a) is not appropriate there) and shears mainly in the vicinity of the bottom, whereas the shear-rate adjacent to the free-surface is low [1,2,17,16,20]. These typical characteristics of rapid granular flows are illustrated by panel (c). So, for such flow configuration, panel (a) and (b) are not applicable, at least in the far downstream. However, we continue our analysis also with the no-slip boundary condition (panel (a)), because locally granular flow can behave as a no-slip material in the vicinity of the silo gate, in strong flow obstacle interactions, in the deposition, and in situations when the channel inclination is at or below the basal friction angle and when the basal surface is rough (e.g., glued with the same material). In the later cases, the flow sticks at the basal surface and the flow is slow or creeping. Panel b of Fig. 6 indicates that free-slip is not a right candidate as there is no velocity structure and the velocity magnitude is also much higher as compared to panels a and c.

The tangential surface and bottom velocities behave completely differently under the change of friction law, Fig. 7. For the Coulomb friction law (with $\delta = 25°$) the bottom velocity is non-zero (dotted green[1] line), contrary to the same with the no-slip boundary condition (solid red line), and illustrates a quick decrease near the silo inlet followed by a quick increase along the channel. The decline in the bottom velocity in the vicinity of the inlet ($\hat{x} < 0.1$) reveals the high bottom pressure in this region (see Fig. 11a). The free surface velocities (dashed green and dot-dashed red line) increases rapidly in the beginning ($\hat{x} < 0.3$) for both friction laws, Fig. 7. However, the no-slip boundary condition generates a very strong, velocity-dependent friction, which afterwards almost compensates the gravitational acceleration, and hence the free surface velocity grows very slowly (dot-dashed red line).

The different friction laws result not only in different shear profiles but also in different mean flow velocities and heights (depths), which are shown in Figs. 8 and 9, respectively. The mean flow velocity strongly depends on the frictional resistance at the bottom, e.g., the mean velocity at the end of the channel for the Coulomb friction with $\delta = 25°$ is roughly double the one for the no-slip boundary condition. Simulations using the Coulomb sliding law generate mean velocities which are controlled by the bed friction angle and are always higher than the mean velocities induced by the no-slip boundary condition. This also affects the flow heights (Fig. 9), which are inversely correlated to the velocity by the continuity condition. The increase of flow depth, averaged along the channel with length L, $\mathcal{H} = 1/L \int_0^L h dx$, with rising bed friction angle is shown in Fig. 10. It can be described by a simple power law function, $\mathcal{H}(\tan\delta)/H = a(\tan\delta)^n + b$, with $a = 0.19$, $b = 0.38$ and $n = 1.3$. This demonstrates that the choice of the boundary condition and the friction coefficient substantially influences the flow dynamics. However, the rate at which the mean velocity increases and depth decreases depends on the ratio of the driving force (gravity) to the resisting forces (e.g., bottom friction). If the bottom

[1] For interpretation of color in Figs. 4–9, 11–22, the reader is referred to the web version of this article.

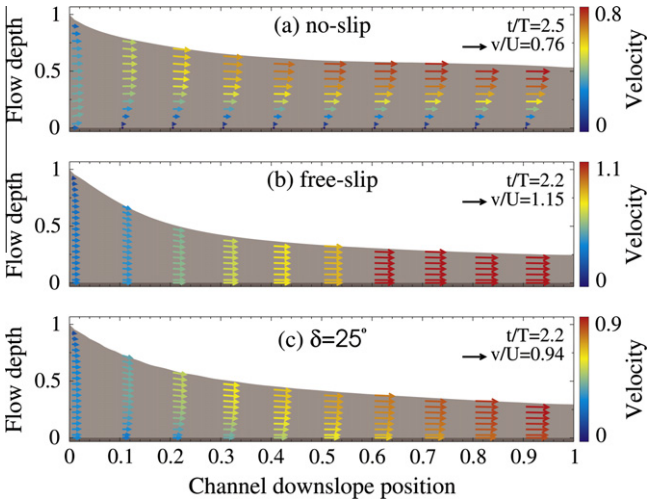

Fig. 6. Full two-dimensional velocity vectors at different channel positions for three different basal friction laws: no-slip (a), free-slip (b), and Coulomb friction law (c) with $\delta = 25°$. The flow enters the channel at $x = 0$ with an average velocity of $\bar{u}^{in}/U = 0.29$. The background grey colour represents the flow depth. All quantities are dimensionless.

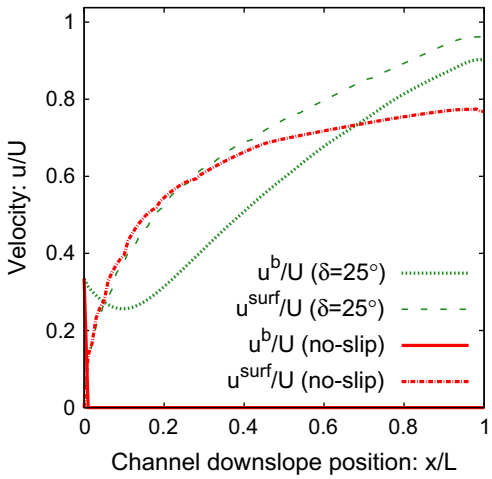

Fig. 7. Dimensionless surface and bottom velocities, u^{surf}/U and u^{b}/U, along the channel for no-slip and Coulomb friction law with $\delta = 25°$.

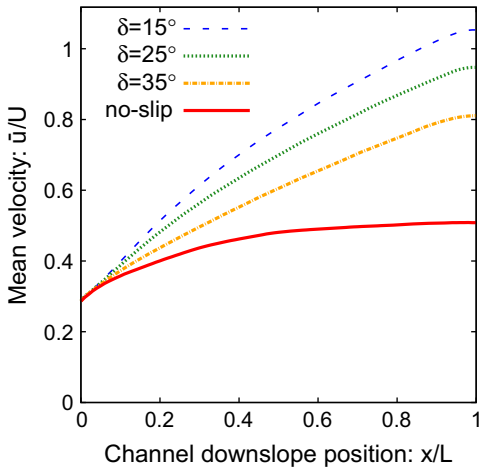

Fig. 8. Dimensionless mean velocity $\bar{u}/U$ along the channel for different basal friction laws.

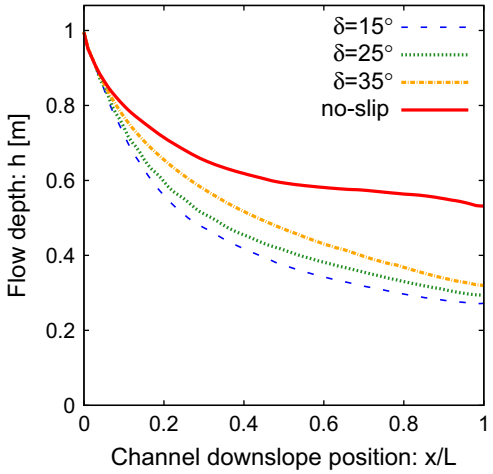

Fig. 9. Dimensionless flow depth h/H along the channel for different basal friction laws.

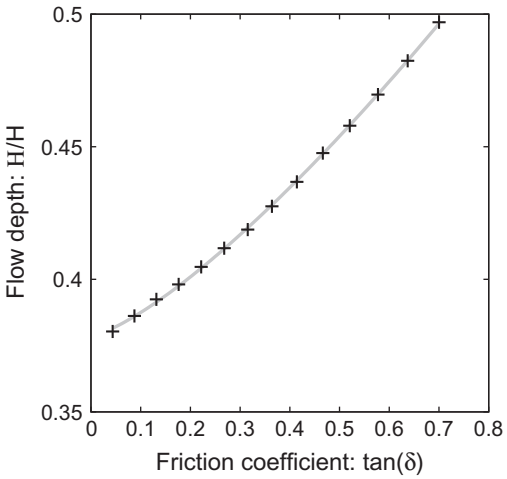

Fig. 10. Dimensionless flow depth $\mathcal{H}/H$ (averaged through the channel length) for different friction coefficients $\tan\delta$. The flow depths simulated with the Coulomb-viscoplastic sliding model are illustrated by plus marks. The grey line corresponds to a power law function, $\mathcal{H}(\tan\delta)/H = a(\tan\delta)^n + b$, with $a = 0.19$, $b = 0.38$ and $n = 1.3$.

friction increases with the flow velocity, the (mean) velocity will saturate at some distance from the silo inlet. This is observed for no-slip flows. We are considering "dry" friction which does not depend on the velocity. A velocity-dependence can be included in the bottom friction by adding the term $c_u u^2$ to the right-hand side of (10) [2]. This becomes eventually important in describing snow avalanches which may show a uniform flow (constant flow height) over a wide range of slope angles [16,20].

In Fig. 11a and b the pressure fields, for the Coulomb friction law with $\delta = 25°$ and the no-slip boundary condition, are presented. Although both friction laws show completely different behaviour, for both the pressure exhibits a layered structure along the channel, which originates from the depth-dependence of the pressure and the flow dynamics, see (9). In case of the Coulomb boundary condition, the pressure first increases along x, due to the considerable fall in flow depth, which goes along with a compressional mode of the material near the silo inlet. Later on, the pressure decreases along the channel, because the gravitational acceleration causes a dilatational downslope motion. The latter is not observed for the no-slip boundary condition, because here the frictional

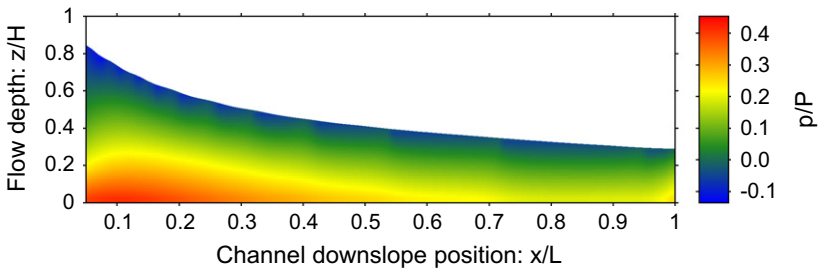

(a) Coulomb friction law with $\delta = 25°$.

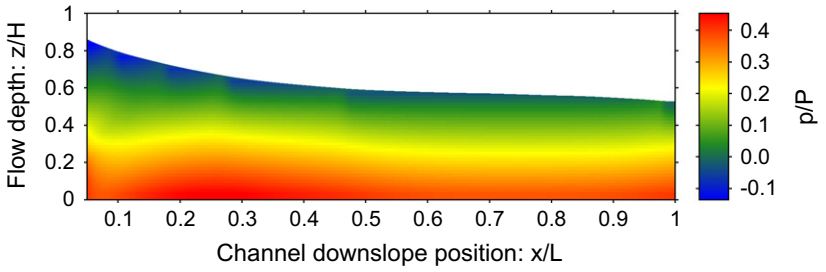

(b) No-slip boundary condition.

Fig. 11. Dimensionless pressure field p/P for Coulomb friction law with $\delta = 25°$ (a), and no-slip boundary condition (b).

resistance at the bottom depends on the tangential velocity and opposes the gravitational acceleration. So, with no-slip, pressure does not vary much along the downslope direction. It is important to note that the pressures here are the full dynamic pressures in contrast to the usual hydrostatic pressure often dealt with in granular flows and mass flows, such as avalanches and debris flows. The full dynamic pressure p can be expressed as a sum of the hydrostatic (p_H) and the dynamic (p_D) pressure: $p = p_H + p_D$, where $p_H = \rho g \cos\zeta(h - z)$ with the flow height h. We see from Fig. 12 that dynamic pressure is important in granular flows. Due to the extensional motion of the granular material in the channel, the hydrostatic pressure significantly overestimates the full pressure p. This becomes clearly visible near the silo inlet. Except in the vicinity of the silo inlet, the dynamic pressure is almost uniform through the flow depth. Analysis of such phenomena is made possible with the full dimensional consideration of the flow.

The previous discussion of Fig. 6 has indicated that the (xz-) shear profile varies along the channel differently depending on the friction law. This becomes clear in Fig. 13, in which the shearing, characterised by $\bar{\dot{\gamma}} = (u^{\text{surf}} - u^{\text{b}})/h$, is presented at different positions in the channel, where u^{s} is the tangential surface velocity, u^{b} is the tangential bottom velocity, and h the flow depth. Therefore, the mean shear-rate $\bar{\dot{\gamma}}$ is an appropriate representative quantity to characterise the interaction of the flowing material with the bottom surface and to distinguish between the different friction laws. The no-slip boundary condition leads to a continuously increasing shearing, see Fig. 7 (for velocities) and Fig. 9 (for heights), compared to the pressure-dependent Coulomb sliding law, for which shearing reaches its maximum value after a certain distance from the inlet (for $\delta = 25°$ at about $\hat{x} = 0.3$) and afterwards it drops slowly. This is compatible with the pressure distribution in Fig. 11a. For both friction laws and all δ values, negative values of $\bar{\dot{\gamma}}$ are observed in the vicinity of the silo inlet. These result from the inflow boundary conditions, see Section 4.1. The shear-rate increases substantially with rising basal friction angle, which controls the frictional strength. Coulomb friction seems to be the more appropriate one for granular flow simulations, whose strength depends on and increases with the material friction.

The variation of the tangential velocity, u, with the flow normal direction z has a completely different characteristic for the simulation with Coulomb friction law as compared to the same with the no-slip boundary condition, see Fig. 14a and b and also Fig. 15a and b. Both simulations show a shear layer near the bottom, which fluently merge into a sliding layer for channel positions at some distant from the inlet ($\hat{x} \geqslant 0.1$). The results in Fig. 14b are similar to the fully two-dimensional plane velocity field through the depth and along the channel as derived analytically by Pudasaini [46]. In contrast to the no-slip, for Coulomb friction law observable shearing mainly takes place close to the sliding surface in agreement with the experimental observations. Furthermore, we observe that

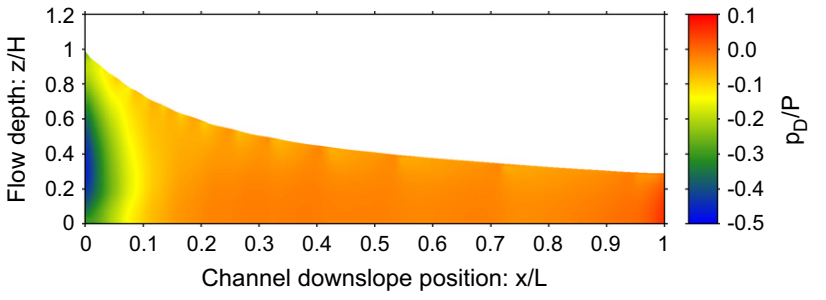

Fig. 12. Dimensionless dynamic pressure, where $p_D = p - p_H$ and $p_H = \rho g \cos\zeta(h - z)$, for Coulomb friction law with $\delta = 25°$.

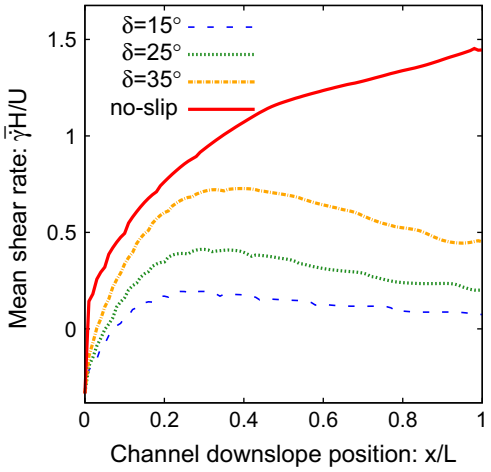

Fig. 13. Dimensionless mean shear rate, with $\bar{\dot{\gamma}} = (u^{\text{surf}} - u^{\text{b}})/h$, along the channel for Coulomb friction, with $\delta = (15°, 25°, 35°)$, and no-slip basal friction laws.

the shear-stress at the bottom increases along the channel, in the case of the no-slip boundary condition, but decreases slightly in the far downstream if the Coulomb sliding law is used. This is experimentally confirmed for snow avalanches by Upadhyay et al. [47].

The Froude number (Fr) is an important non-dimensional number that characterises the dynamics of free surface gravity flows [48,49]. It distinguishes subcritical (slow), critical, and supercritical (rapid) flow regimes, depending on whether Fr is less than, equal to, or greater than unity. Classically, in channel flows of water or granular flows in inclined channels, Fr is defined as the ratio between the inertial and gravity forces or equivalently between the kinetic and potential energies. It is used to establish dynamical similarities between the full-scale and laboratory-scale flows, e.g., in designing the avalanche protection dam and weir [49]. Here, we consider the extended Froude number [7], which includes both the pressure potential and gravity potential energies. We further generalise the extended Froude number for non-depth averaged flows and call it 'generalised Froude number':

$$\text{Fr} = \sqrt{\frac{(u^2 + w^2)}{g[(L - x)\sin\zeta + z\cos\zeta] + p/\rho}}. \tag{30}$$

Here, $u^2 + w^2$ is twice the (two-dimensional) kinetic energy, $g(L - x)\sin\zeta$ is the potential energy caused by the downslope gravitational acceleration, $gz\cos\zeta$ is the potential energy caused by the gravitational acceleration along the flow depth, and p/ρ is the pressure potential energy (all energies are considered per unit mass). For $w = 0$, $z = 0$ and p defined by the hydrostatic pressure, (30) degenerates into the extended Froude number defined in [7].

The advantage of the generalised Froude number is that the whole spectrum of the Froude number through the flow depth and down the entire channel is available. Following [7], the reference level for the potential energy lies at the bottom surface at the end of the channel. In Fig. 16 we observe that the Froude number increases along the downslope position, because the kinetic energy increases, due to gravitational acceleration, and the potential energy decreases. While moving from the bottom to the free-surface of the flow, the Froude number increases, although this holds also for the potential energy. This is, because of the frictional resistance at the bottom, which leads to a strong increase of the kinetic energy in the direction of the free-surface the flow depth. So, in general, the Froude number is not uniform through depth.

At $\hat{x} = 0.4$ the Froude number is approximately one, and the flow pass from the subcritical to the supercritical regime. Therefore, granular flows on inclined surfaces are characteristically rapid supercritical flows. However, note that as viewed from the bottom surface, the flow regime is slightly curved to the upstream and then straight at the top of the free-surface. It can be observed by following the central part of the yellow zone.

4.2.2. Parameter studies

In this section the influence of the physical parameters ζ (channel inclination), ν (kinematic viscosity), $\bar{u}^{\text{in}}$ (mean inflow velocity) and h^{in} (inflow height) on the shear-rate parameter $\bar{\dot{\gamma}}$ is studied for both quasi-steady-state flows obeying the Coulomb friction law with a bed friction angle of $\delta = 25°$ and flows subject to the no-slip boundary condition. It is observed in Fig. 13 that the shear-rate parameter lines $\bar{\dot{\gamma}}(x)$ do not cross each other for the simulations with different friction laws. This holds also for simulations which differ in one of the physical parameters. Therefore, the value of $\bar{\dot{\gamma}}$ at the middle of the channel ($\hat{x} = 0.5$), $\bar{\dot{\gamma}}^{\text{c}}$, can be considered as a characteristic value for the entire friction law with a given parameter. The advantage of $\bar{\dot{\gamma}}^{\text{c}}$ is its negligible dependency on the inflow and outflow boundary conditions.

Fig. 17 shows the fall of $\bar{\dot{\gamma}}^{\text{c}}$ for rising inclination angles ζ for Coulomb friction law. On the one hand, the decreasing gravitational force normal to the bottom surface ($\propto\cos\zeta$) leads to a reduction of the bottom normal stress. On the other hand, the increasing gravitational force parallel to the bottom surface ($\propto\sin\zeta$) results in an additional acceleration of the flow and hence enhances flow

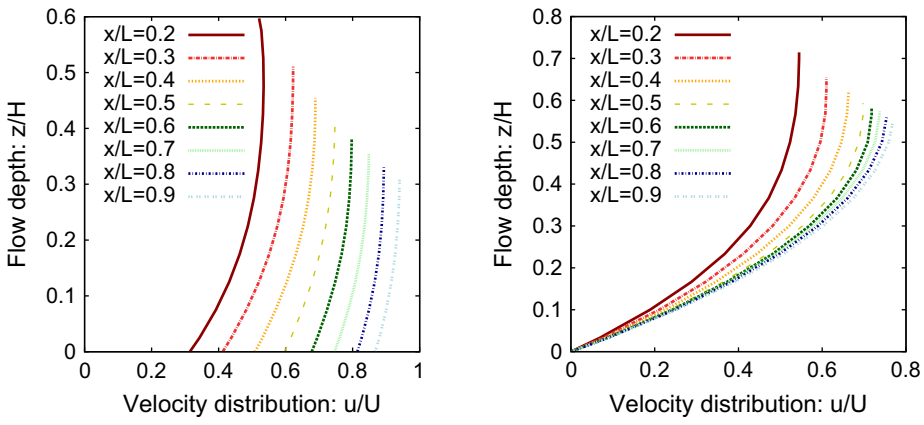

(a) Coulomb friction law with $\delta = 25°$. (b) No-slip boundary condition.

Fig. 14. Non-dimensionalised velocity distribution through depth at different channel positions for Coulomb friction law with $\delta = 25°$ (a), and no-slip boundary condition (b).

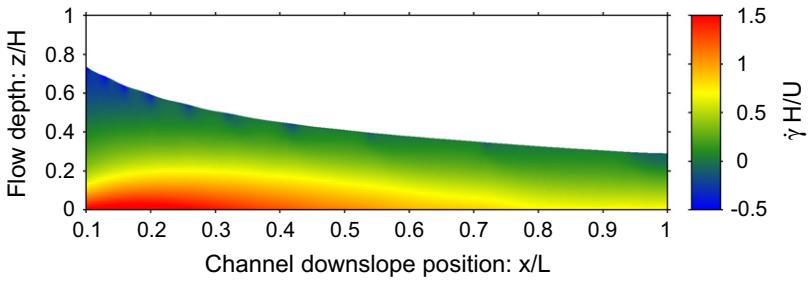

(a) Coulomb friction law with $\delta = 25°$.

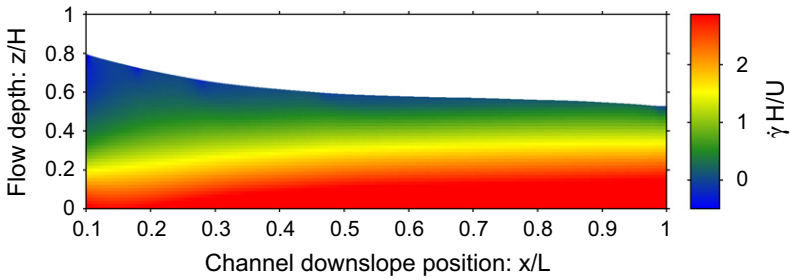

(b) No-slip boundary condition.

Fig. 15. Non-dimensionalised gradient of the tangential velocity in direction normal to the bottom surface, i.e., the shear-rate $\dot{\gamma} = \partial_z u$, for channel positions for Coulomb friction law with $\delta = 25°$ (a) and no-slip boundary condition (b).

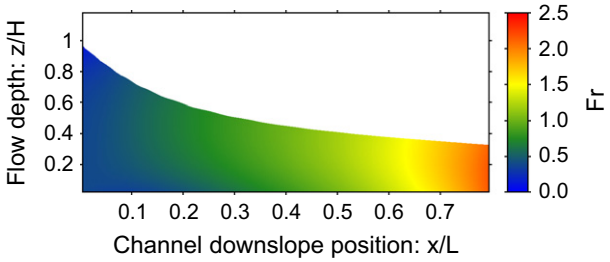

Fig. 16. Generalised Froude number for Coulomb friction law with $\delta = 25°$.

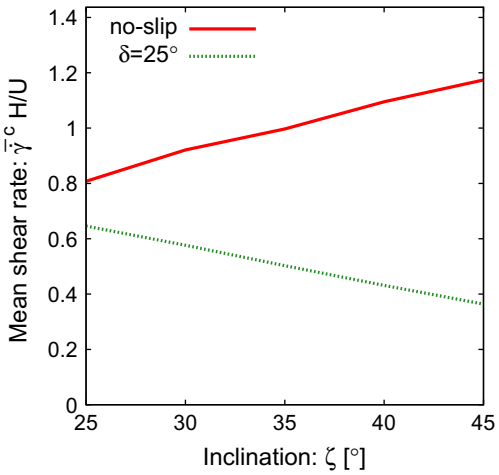

Fig. 17. Dimensionless shearing parameter $\bar{\dot{\gamma}}^c H/U$ for steady state flows in a rectangular channel with varied inclination angles. The frictional resistance at the bottom is described by the Coulomb friction law with a bed friction angle of $\delta = 25°$ (dotted green line) and the no-slip boundary condition (solid red line), respectively.

velocities and lower flow depth. For the Coulomb friction the bottom normal stress defines the bottom shear-stress. Therefore, the bottom velocity grows more quickly than the surface velocity, and the bottom shear-rate, and also the mean shear-rate $\bar{\dot{\gamma}}$, decreases with increasing inclination angle. No-slip flows, for which the frictional resistance is not connected to the bottom normal stress, show an inverse behaviour: The shear-rate increases with the inclination angle, because the bottom velocity remains zero independent of the inclination angle. Consequently, the drop of the shear-rate with increasing inclination is characteristic for the (dry) Coulomb friction law. However, Rognon et al. showed for chute flow experiments with snow that the shear-rate increases with inclination, at which a non-zero sliding velocity is observed [20]. This indicates a velocity-dependent friction component, which may result from the roughness of the bottom surface as the channel bottom was covered with sand paper. This shows that the inclusion of drag in the basal sliding law may become necessary in some situations [50].

The viscosity is a measure of the resistance against deformation, e.g., induced by the frictional force at the bottom, and high viscosity means a high resistance. Therefore, a rise in viscosity leads to a decrease in mean and surface flow velocities and hence an increase in flow depth. However, for Coulomb friction the bottom velocity shows a different behaviour compared to the surface velocity: It grows with rising viscosity, because of a lower amount of transfer of the shear-stress exerted by the bottom surface into the granular material. Note that the bottom shear-stress, which is induced by the Coulomb friction or the no-slip boundary condition, is viscosity-dependent. This dependency is positive and weaker than a linear relation. As a consequence, for both the Coulomb friction and the no-slip boundary condition, the shear-rate $\bar{\dot{\gamma}}$ decreases with increasing viscosity, Fig. 18. The decrease is faster for the Coulomb friction due to its weaker viscosity-dependency. For a given viscosity, shear-rate in Coulomb-sliding is less than the same with no-slip boundary condition.

In Fig. 19, the dependence of $\bar{\dot{\gamma}}^c$ on the mean inflow velocity $\bar{u}^{in}$ is illustrated. If the material is fed with higher velocity, the mean and surface velocity along the channel and also the flow depth will

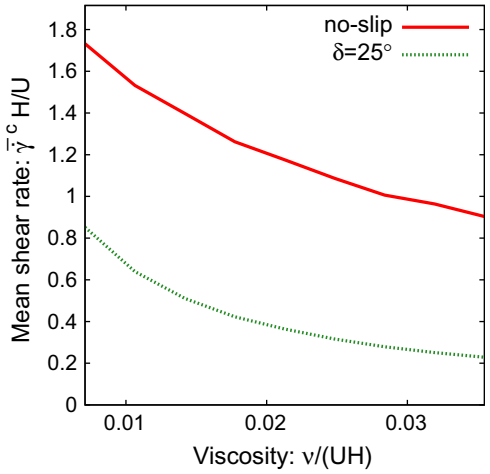

Fig. 18. Dimensionless shearing parameter $\bar{\dot{\gamma}}^c H/U$ for steady state flows with varied dimensionless viscosities $\nu/(UH)$. The frictional resistance at the bottom is described by the Coulomb friction law with a bed friction angle of $\delta = 25°$ (dotted green line) and the no-slip boundary condition (solid red line), respectively.

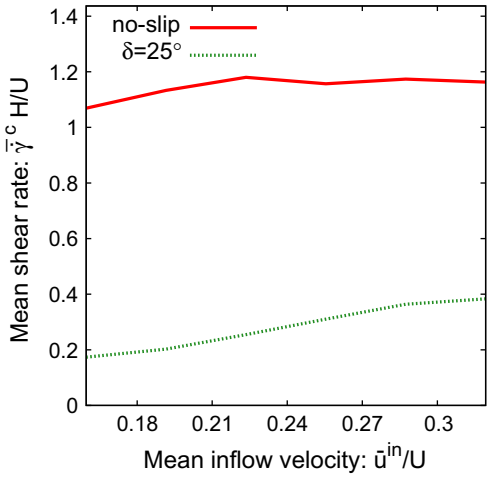

Fig. 19. Dimensionless shearing parameter $\bar{\dot{\gamma}}^c H/U$ for steady state flows with varied dimensionless inflow velocities $\bar{u}^{in}/U$. The frictional resistance at the bottom is described by the Coulomb friction law with a bed friction angle of $\delta = 25°$ (dotted green line) and the no-slip boundary condition (solid red line), respectively.

rise. However, for the Coulomb friction the bottom velocity is negatively correlated with the bottom normal stress, which increases due to the growth in depth. Therefore, the bottom shear-rate increases substantially with rising inflow velocities and hence the mean shear-rate $\bar{\dot{\gamma}}$ for the Coulomb friction law. For the no-slip boundary condition the variation of the inflow velocity generates a slight change in the bottom shear-rate, and, consequently, the mean shear-rate shows a moderate increase, decrease respectively, with rising $\bar{\dot{\gamma}}$ if the change in the free surface velocity dominates the change in the flow depth, or vice versa respectively. Note that an increase or decrease of the Coulomb friction angle will respectively amplify or soften the change of the mean shear-rate with the physical property due to (10).

4.3. Flow evolution

In this section, the time dependence of the flow is examined. This is important to describe the overall flow dynamics and the temporal and spatial variations of the flow depth and the velocity distributions through the flow depth. Here, we investigate the complete flow evolution from the flow release from the silo gate down the entire channel. This will be done for all three frictional resistances and the results are compared.

In Fig. 20, snapshots of the velocity fields are shown for the no-slip boundary condition. In panel (a) (at time $\hat{t} = 0.3$) the maximum front velocity is located at the middle height of the front ($\hat{z} \approx 0.3$). With time (panels b-f), the free surface of the flow front becomes the fastest flowing region as a result of the strong frictional resistance at the bottom. As a consequence, the flow front deforms only marginally. The free-slip boundary condition leads to completely different velocity fields and flow heights due to the missing friction at the bottom, Fig. 21. At all timesteps the maximum front velocity is located at the bottom. However, the velocity differs only slightly through the depth. The front shape is more diffusive compared to the no-slip flow.

The evolution of the flow with time for the Coulomb friction with $\delta = 25°$ is presented in Fig. 22. For some times, panels (a)–(c), the maximum velocity is located at the front head, somewhere between the free surface and the bottom surface. For later times, panels (d)–(f), the vertical position of the maximum velocity is close to the free surface at the forehead. So, it shows the evolution of the maximum velocity region within the sliding and dynamically evolving material. As time elapses, the flow front becomes more and more diffusive and the (xz-) shearing becomes more visible. Compared to the other friction laws (Figs. 20 and 21), the diffusion and the flow height lies between the one produced by the free-slip and the one of the no-slip boundary condition.

This demonstrates that the no-slip, free-slip and Coulomb friction boundary conditions do not only lead to completely different flow properties, when a quasi-steady-state flow is considered, but also during the whole temporal evolution of the flow. The results with Coulomb friction law are in line with our physical intuition and some observed phenomena.

5. Discussions and summary

Flow dynamical quantities, e.g., depth, velocities and pressure, play a crucial role for the construction of defence structures, hazard mitigation in disaster prone mountain regions, and also in the transportation of granular material in process engineering. Therefore, in general, we need a physically complete description of the flow dynamics without reduction of the information through the flow depth. It is observed in experiments and in the field that in rapid flow of granular material down the slopes even the lowest particle layer in contact with the bottom boundary moves with a non-zero and non-trivial velocity. Hence, appropriate rheology, boundary conditions, and numerical methods are required in order to properly determine the flow dynamics associated with geophysical and industrial mass flows, such as avalanches, debris flows, and flow of granular materials. Explicit knowledge of the dynamic and variable basal slip was skipped in depth-averaged models and simulation due to depth-averaging.

We developed a fully two-dimensional, novel Coulomb-viscoplastic sliding model, which includes some basic features and observed phenomena in dense granular flows like the exhibition of a yield strength and a non-zero slip velocity. The internal deformation is modelled as a viscoplastic material. The interaction of the flow with the solid boundary is described by the pressure and rate-dependent Coulomb-viscoplastic sliding law, which relates the shear-stress to the normal stress at the boundary. This relation is linear and defined by the bed friction angle. The non-hydrostatic and full dynamic pressures is modelled as a Poisson equation in terms of the flow dynamic and gravity forces, including the material friction, viscous, and strength parameters. The numerical treatment of the Coulomb-viscoplastic sliding model requires the set up

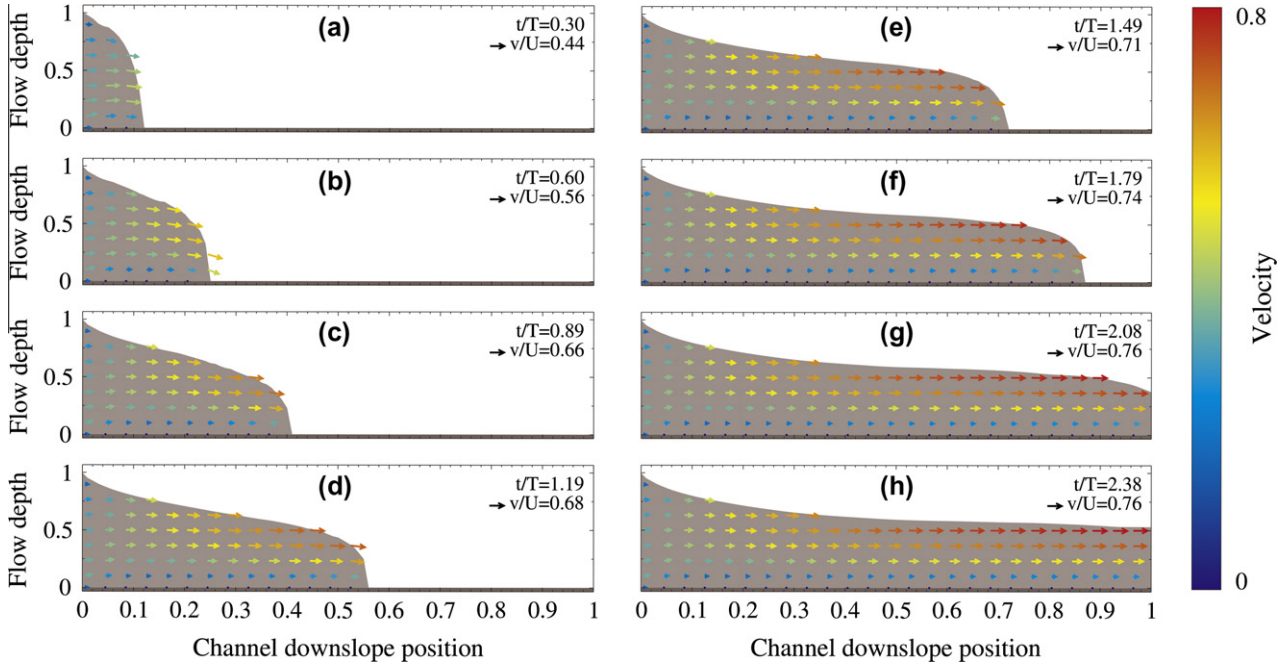

Fig. 20. Snapshots of rapidly flowing granular material down a steep rectangular open channel. The interaction of the fluid with the channel bottom is modelled by the no-slip boundary condition.

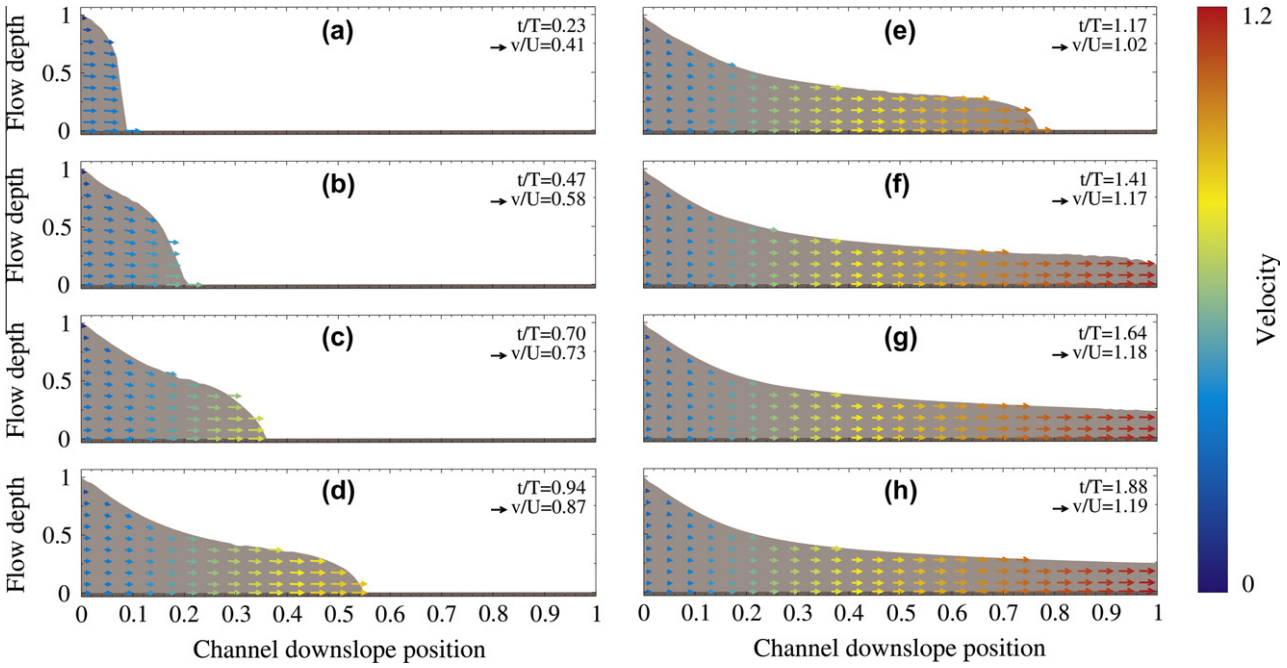

Fig. 21. Snapshots of rapidly flowing granular material down a steep rectangular open channel. The interaction of the fluid with the channel bottom is modelled by the free-slip boundary condition.

of a novel pressure equation, which defines the pressure independently of the bottom boundary velocities. These are dynamically and automatically defined for given pressure by the Coulomb-viscoplastic sliding law, which we numerically implemented for the first time. This represents an entirely novel and innovative concept in rapid granular flows both from a physical modelling and a computational point of view. To simulate and visualise the rapid free surface flow of frictional granular material, the marker-and-cell method is applied. With the new model we can simulate the entire flow dynamics and the flow depth variations of the field quantities, mainly the velocity and full dynamic pressure, and also other derived quantities, such as the shear-rate, and dynamic pressure. Furthermore, it provides a complete dynamical description of the time and spatial evolution of the basal boundary slip velocity, which was lacking in the literature.

We numerically studied the fully two-dimensional inclined channel flow for three different basal boundary conditions: no-slip, free-slip and the Coulomb-type slip at the base. We showed that the choice of the bottom boundary is very crucial as it can fundamentally alter the flow dynamics. The Coulomb sliding law leads

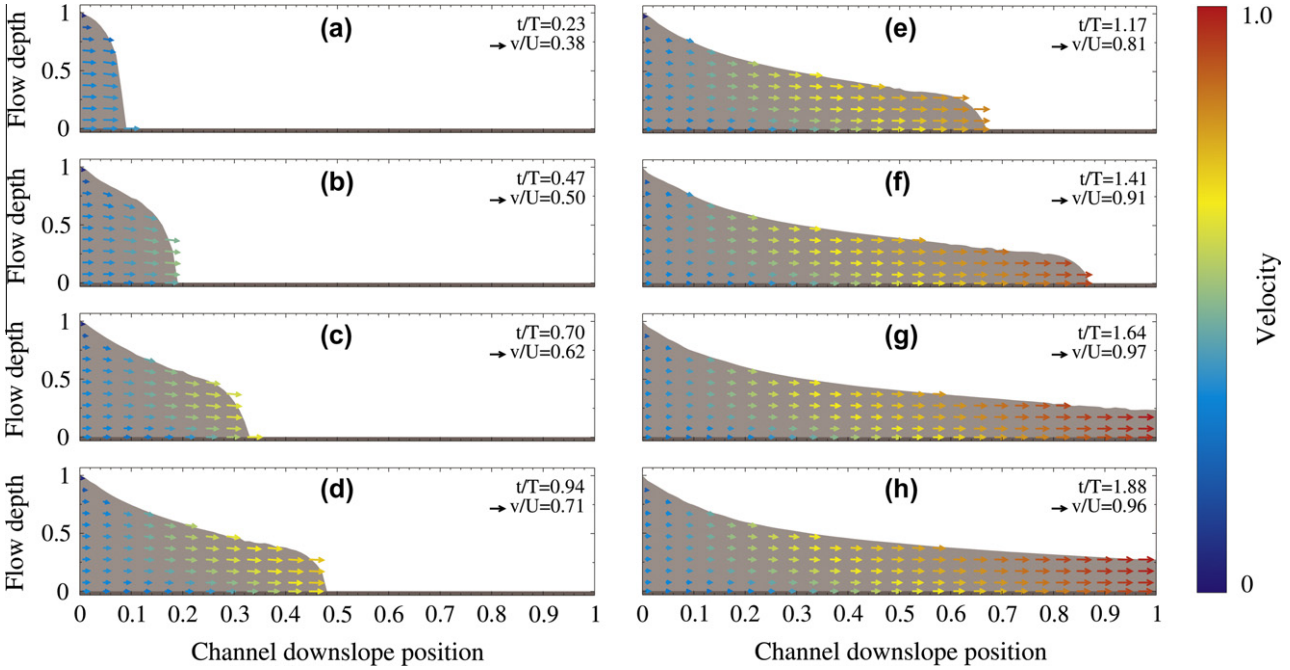

Fig. 22. Snapshots of rapidly flowing granular material down a steep rectangular open channel. The interaction of the fluid with the channel bottom is modelled by the Coulomb friction law with $\delta = 25°$.

to non-vanishing slip velocities and to completely different distributions of the flow height and velocities than those obtained with usual boundary conditions like the no-slip boundary condition. The latter are unphysical for many frictional flows, especially for granular materials as observed in experiments and in the field. This means that the bottom boundary condition is an important mechanism to appropriately control and describe the flow dynamics in rapid granular flows in steep channels. It is demonstrated that high bed friction angles go along with a strong shearing. In reality the bed friction angle depends on both the granular material and the boundary substrate. We showed that for Coulomb friction law observable shearing mainly takes place close to the sliding surface in agreement with observations. This cannot be modelled by classical free-slip and no-slip boundary conditions. Furthermore, we observed that the bottom shear-stress increases along the channel, in the case of the no-slip boundary condition, but decreases slightly in the far downstream if the Coulomb sliding law is used. We defined the general Froude number for a fully two-dimensional inclined channel flow and showed that it increases with downslope positions and also while moving from the bottom to the free-surface. In general, the Froude number is not uniform through the depth. The analysis of the Froude number showed that granular flows on inclined surfaces are characteristically rapid supercritical flows. Also the no-slip and the Coulomb friction law simulations show completely different results for the variation of the inclination angle, which reveals that the drop of the shear-rate with increasing inclination is characteristic of the Coulomb friction law. This is usefull to classify the flow regimes in laboratory experiments and field events. We showed that the simulated full dynamic pressure differs considerably from the hydrostatic pressure, which is used in classical avalanche and granular flow models. In extensional flow regimes the hydrostatic pressure largely overestimates the full dynamic pressure, whereas we expect that for strong compressional flows, e.g., in the vicinity of flow obstacle interaction, an underestimation may be observed. This is particularly critical for the construction of defence structures in disaster prone mountain regions. Comparison of the simulation results with observed data will be presented later.

Acknowledgements

We thank the German Research Foundation (DFG) for the financial support through Contract No. PU 386/1-1,2: Transition of a granular flow into the deposit. Special thanks are also due to the editor, Roland Keunings, and the anonymous reviewers for their constructive reviews that helped to improve the quality of the paper.

References

[1] S. Pudasaini, K. Hutter, S. Hsiau, S. Tai, Y. Wang, R. Katzenbach, Rapid flow of dry granular materials down inclined chutes impinging on rigid walls, Phys. Fluids 19 (2007) 053302.
[2] S. Pudasaini, K. Hutter, Avalanche Dynamics: Dynamics of Rapid Flows of Dense Granular Avalanches, Springer, Berlin, New York, 2007.
[3] S. Savage, K. Hutter, The motion of a finite mass of granular material down a rough incline, J. Fluid Mech. 199 (1989) 177–215.
[4] J. Gray, M. Wieland, K. Hutter, Gravity-driven free surface flow of granular avalanches over complex basal topography, Proc. R. Soc. Lond. Ser. A 455 (1999) 1841.
[5] S. Pudasaini, Y. Wang, L. Sheng, K. Hutter, R. Katzenbach, Avalanching granular flows down curved and twisted channels: theoretical and experimental results, Phys. Fluids 20 (2008) 073302.
[6] S. Pudasaini, C. Kröner, Shock waves in rapid flows of dense granular materials: theoretical predictions and experimental results, Phys. Rev. E 78 (2008) 041308.
[7] S. Pudasaini, B. Domnik, Energy considerations in accelerating rapid shear granular flows, Nonlin. Process. Geophys. 16 (2009) 399–407.
[8] C. Fang, Y. Wang, K. Hutter, A unified evolution equation for the cauchy stress tensor of an isotropic elasto–visco-plastic material, Contin. Mech. Thermodyn. 19 (2008) 423–440.
[9] C. Ancey, Plasticity and geophysical flows: a review, J. Non-Newton. Fluid Mech. 142 (2007) 4–35.
[10] Y. Forterre, O. Pouliquen, Flows of dense granular media, Annu. Rev. Fluid Mech. 40 (2008) 1–24.
[11] S. Goldstein, Modern Developments in Fluid Dynamics, Clarendon Press, Oxford, 1938.
[12] M. Griebel, T. Dornseifer, T. Neunhoeffer, Numerical Simulation in Fluid Dynamics: A Practical Introduction, Society for Industrial and Applied Mathematics, Philadelphia, 1997.
[13] C. Hartel, E. Meiburg, F. Necker, Analysis and direct numerical simulation of the flow at a gravity-current head. part 1. Flow topology and front speed for slip and no-slip boundaries, J. Fluid Mech. 418 (2000) 189–212.

[14] Y. Liu, X. Liu, E. Wu, Real-time 3d fluid simulation on gpu with complex obstacles, in: 12th Pacific Conference on Computer Graphics and Applications, Seoul, South Korea, 6–8 October 2004, pp. 247–256.
[15] M. Massoudi, T. Phuoc, The effect of slip boundary condition on the flow of granular materials: a continuum approach, Int. J. Non-Lin. Mech. 35 (2000) 745–761.
[16] M. Kern, F. Tiefenbacher, J. McElwaine, The rheology of snow in large chute flows, Cold Reg. Sci. Technol. 39 (2004) 181–192.
[17] S. Pudasaini, Y. Wang, K. Hutter, Velocity measurements in dry granular avalanches using particle image velocimetry technique and comparison with theoretical predictions, Phys. Fluids 17 (2005) 093301.
[18] K. Platzer, P. Bartelt, C. Jaedicke, Basal shear and normal stresses of dry and wet snow avalanches after a slope deviation, Cold Reg. Sci. Technol. 49 (2007) 11–25.
[19] K. Platzer, P. Bartelt, M. Kern, Measurements of dense snow avalanche basal shear to normal stress ratios (s/n), Geophys. Res. Lett. 34 (2007) L07501.
[20] P. Rognon, F. Chevoir, H. Bellot, F. Ousset, M. Naaïm, P. Coussot, Rheology of dense snow flows: inferences from steady state chute-flow experiments, J. Rheol. 52 (2008) 729.
[21] L. Leger, H. Hervet, G. Massey, E. Durliat, Wall slip in polymer melts, J. Phys.: Condens. Matter 9 (1997) 7719–7740.
[22] W. Schowalter, The behavior of complex fluids at solid boundaries, J. Non-Newton. Fluid Mech. 29 (1988) 25–36.
[23] S. Granick, Y. Zhu, H. Lee, Slippery questions about complex fluids flowing past solids, Nat. Mater. 2 (2003) 221–227.
[24] R. Kerswell, Dam break with coulomb friction: a model for granular slumping?, Phys Fluids 17 (2005) 057101.
[25] U. Gruber, P. Bartelt, Snow avalanche hazard modelling of large areas using shallow water numerical methods and gis, Environ. Modell. Softw. 22 (2007) 1472–1481.
[26] M. Naaim, S. Vial, R. Couture, Saint-venant approach for rock avalanches modelling, in: Saint Venant Symposium, Paris, pp. 28–29.
[27] E. Uhland, Modell zur beschreibung des fließens wandgleitender substanzen durch düsen, Rheol. Acta 15 (1976) 30–39.
[28] N. Balmforth, I. Frigaard, Viscoplastic fluids: from theory to application, J. Non-Newton. Fluid Mech. 142 (2007) 1–3.
[29] E. Bingham, Fluidity and Plasticity, New York, McGrawHill, 1922.
[30] P. Jop, Y. Forterre, O. Pouliquen, A constitutive law for dense granular flows, Nature 441 (2006) 727–730.
[31] T. Papanastasiou, Flows of materials with yield, J. Rheol. 31 (1987) 385.
[32] K. Whipple, Open-channel flow of bingham fluids: applications in debris-flow research, J. Geol. (1997) 243–262.
[33] J. Dent, T. Lang, Experiments on mechanics of flowing snow, Cold Reg. Sci. Technol. 5 (1982) 253–258.
[34] P. Gauer, A. Elverhoi, D. Issler, F. De Blasio, On numerical simulations of subaqueous slides: back-calculations of laboratory experiments of clay-rich slides, Nor. J. Geol. 86 (2006) 295.
[35] B. Voight, J. Sousa, Lessons from ontake-san: a comparative analysis of debris avalanche dynamics, Eng. Geol. 38 (1994) 261–297.
[36] S. Moriguchi, A. Yashima, K. Sawada, R. Uzuoka, M. Ito, Numerical simulation of flow failure of geomaterials based on fluid dynamics, Soils Found. 45 (2005) 155–165.
[37] F. Harlow, J. Welch, Numerical calculation of time-dependent viscous incompressible flow of fluid with free surface, Phys. Fluids 8 (1965) 2182–2189.
[38] M. Tom, J. Doricio, A. Castelo, J. Cuminato, S. McKee, Solving viscoelastic free surface flows of a second-order fluid using a marker-and-cell approach, Int. J. Num. Meth. Fluids 53 (2007) 599–627.
[39] E. Muravleva, Finite-difference schemes for the computation of viscoplastic medium flows in a channel, Math. Models Comput. Simul. 1 (2009) 768–779.
[40] D. Young, Iterative Solution of Large Linear Systems, Dover Publications, New York, 2003.
[41] T. Takahashi, Debris Flow, IAHR-AIRH Monograph Series A, Balkema, 1991.
[42] T. Takahashi, Debris Flow: Mechanics, Prediction, and Countermeasures, Taylor and Francis, Leiden, 2007.
[43] R. Iverson, The physics of debris flows, Rev. Geophys. 35 (1997) 245–296.
[44] W. Dade, H. Huppert, Long-runout rockfalls, Geol. 26 (1998) 803–806.
[45] T. Davies, M. McSaveney, K. Kelfoun, Runout of the socompa volcanic debris avalanche, chile: a mechanical explanation for low basal shear resistance, Bull. Volcanol. 72 (2010) 933–944.
[46] S. Pudasaini, Some exact solutions for debris and avalanche flows, Phys. Fluids 23 (2011) 043301.
[47] A. Upadhyay, A. Kumar, A. Chaudhary, Velocity measurements of wet snow avalanche on the dhundi snow chute, Ann. Glaciol. 51 (2010) 139–145.
[48] J. Gray, Y.-C. Tai, S. Noelle, Shock waves, dead zones and particle-free regions in rapid granular free-surface flows, J. Fluid Mech. 491 (2003) 161–181.
[49] K. Hákonardóttir, A. Hogg, Oblique shocks in rapid granular flows, Phys. Fluids 17 (2005) 077101.
[50] J. Fischer, J. Kowalski, S. Pudasaini, Topographic curvature effects in applied avalanche modeling, Cold Reg. Sci. Technol. 74–75 (2012) 21–30.